Cell Reports
Physical Science

Article

# Label-free cell imaging and tracking in 3D organoids

## Graphical abstract

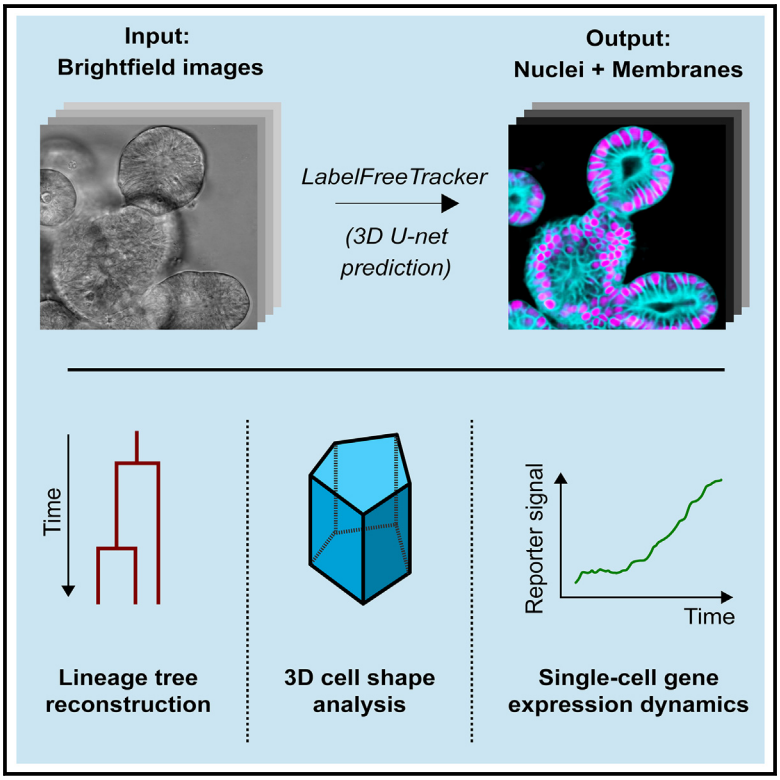


## Highlights

- LabelFreeTracker enables 3D label-free image analysis of intestinal organoids
- Predicts 3D cell membrane and nucleus based on bright-field images
- Allows label-free single-cell tracking over multiple generations
- Provides a tool for quantitative analysis of reporter expression and cell morphology

## Authors

Rutger N.U. Kok, Willem Kasper Spoelstra, Max A. Betjes, Jeroen S. van Zon, Sander J. Tans

## Correspondence

j.v.zon@amolf.nl (J.S.v.Z.), s.tans@amolf.nl (S.J.T.)

## In brief

Kok et al. present the LabelFreeTracker approach for quantitative single-cell tracking analysis in 3D intestinal organoids on the basis of bright-field images. This tool allows for label-free cell counting, lineage tree reconstruction, reporter expression dynamics, and cell shape analysis in intestinal organoids.

Kok et al., 2025, Cell Reports Physical Science 6, 102522
April 16, 2025 
https://doi.org/10.1016/j.xcrp.2025.102522

CellPress

Cell Reports
Physical Science

CellPress
OPEN ACCESS

Article

# Label-free cell imaging and tracking in 3D organoids

Rutger N.U. Kok,[1] Willem Kasper Spoelstra,[1] Max A. Betjes,[1] Jeroen S. van Zon,[1,*] and Sander J. Tans[1,2,3,*]
[1]AMOLF, 1098 XG Amsterdam, the Netherlands
[2]Bionanoscience Department, Kavli Institute of Nanoscience Delft, Delft University of Technology, 2629 HZ Delft, the Netherlands
[3]Lead contact
*Correspondence: j.v.zon@amolf.nl (J.S.v.Z.), s.tans@amolf.nl (S.J.T.)
https://doi.org/10.1016/j.xcrp.2025.102522

## SUMMARY

Fluorescence live-cell microscopy is one of the most frequently used techniques to study dynamic processes in organoids. However, it is often limited by laborious fluorescent reporter engineering, limited numbers of fluorescence channels, and adverse phototoxicity and protein overexpression effects. Label-free imaging is a promising alternative but not yet established for 3D cultures. Here, we introduce LabelFreeTracker, a label-free machine-learning-based method to visualize the nuclei and membranes in bright-field images of 3D mouse intestinal organoids. The approach uses U-Net neural networks trained on the bright-field transmitted light and fluorescence images of mouse intestinal organoids as obtained by standard confocal microscopy. LabelFreeTracker frees up fluorescence channels to study fluorescent reporters and allows (semi-)automated quantification of cell movement, cell shape and volume changes, proliferation, differentiation, and lineage trees. This method greatly simplifies live-cell imaging of tissue dynamics and will accelerate screening of patient-derived organoids, for which reporter engineering is not feasible.

## INTRODUCTION

Organoids are rapidly advancing as a major tool in drug discovery, personalized medicine, and basic research and offer an alternative to animal testing.[1] The dynamics of cell proliferation,[2,3] migration,[4] and differentiation[5] in organoids are critical for understanding normal and pathological development.[6] Furthermore, organoids are rapidly advancing as *in vitro* model systems to study drug responses. Studying dynamics at the single-cell level requires that cells are distinguishable from each other and can be followed over time. This is typically achieved by fluorescent labeling of either the cell nucleus or membrane.[2–5,7–9] However, the required engineering of fluorescent labels is, in practice, unfeasible for many applications, such as screening in patient-derived organoids. Furthermore, the nuclear and membrane labels needed to identify cells in 3D tissues limit the colors available for functional studies, such as monitoring cell fate markers or fluorescence resonance energy transfer sensors over time, while adding to the phototoxicity. Alternatives, such as holographic and hyperspectral imaging, have been developed[10,11] but require specialized equipment that is not broadly available. In contrast, bright-field microscopy is broadly available and is used extensively for imaging overall organoid growth and morphology.[12–16] Besides its general availability, a major advantage of bright-field microscopy is that it has virtually no phototoxic effects on cells in the sample. Machine learning approaches have been used to visualize and track cells in 2D monolayer cultures.[17–19] Organoids, however, are typically several tens of microns thick, which causes strong light scattering by the intervening tissue and obscures cellular features such as nuclei and membranes[10] (Figure 1A, left).

Here, we present LabelFreeTracker, a label-free imaging method to visualize and track cells in 3D organoids using 3D bright-field images as obtained from the transmitted light in standard 3D confocal microscopy (Figure 1A). Using a custom machine learning approach and a min-cost flow solver, it integrates spatial information in 3D from the scattered light to reconstruct cell nuclei and shapes over 50 μm, deep and temporal information to track cells over multiple generations. The method overcomes the substantial tracking challenges in organoids, where cell nuclei are densely packed and move rapidly during division, while tracking cells through cell divisions is prone to errors, and even single errors can cause large-scale alterations to lineage trees. LabelFreeTracker[20] works in conjunction with OrganoidTracker,[9] our custom-built and freely available software tool for single-cell tracking in organoids, and can be used on data acquired with a standard confocal microscope. Furthermore, LabelFreeTracker can be readily extended to other organoid systems and cellular features. It will enable the analysis of dynamic processes in patient-derived and other organoids when nuclear and membrane labels are not available.

## RESULTS

### The LabelFreeTracker structure

To train LabelFreeTracker, we used a dataset of 3,894 paired bright-field/nuclear fluorescence images from 22 organoids and bright-field/membrane fluorescence images from 25 organoids,

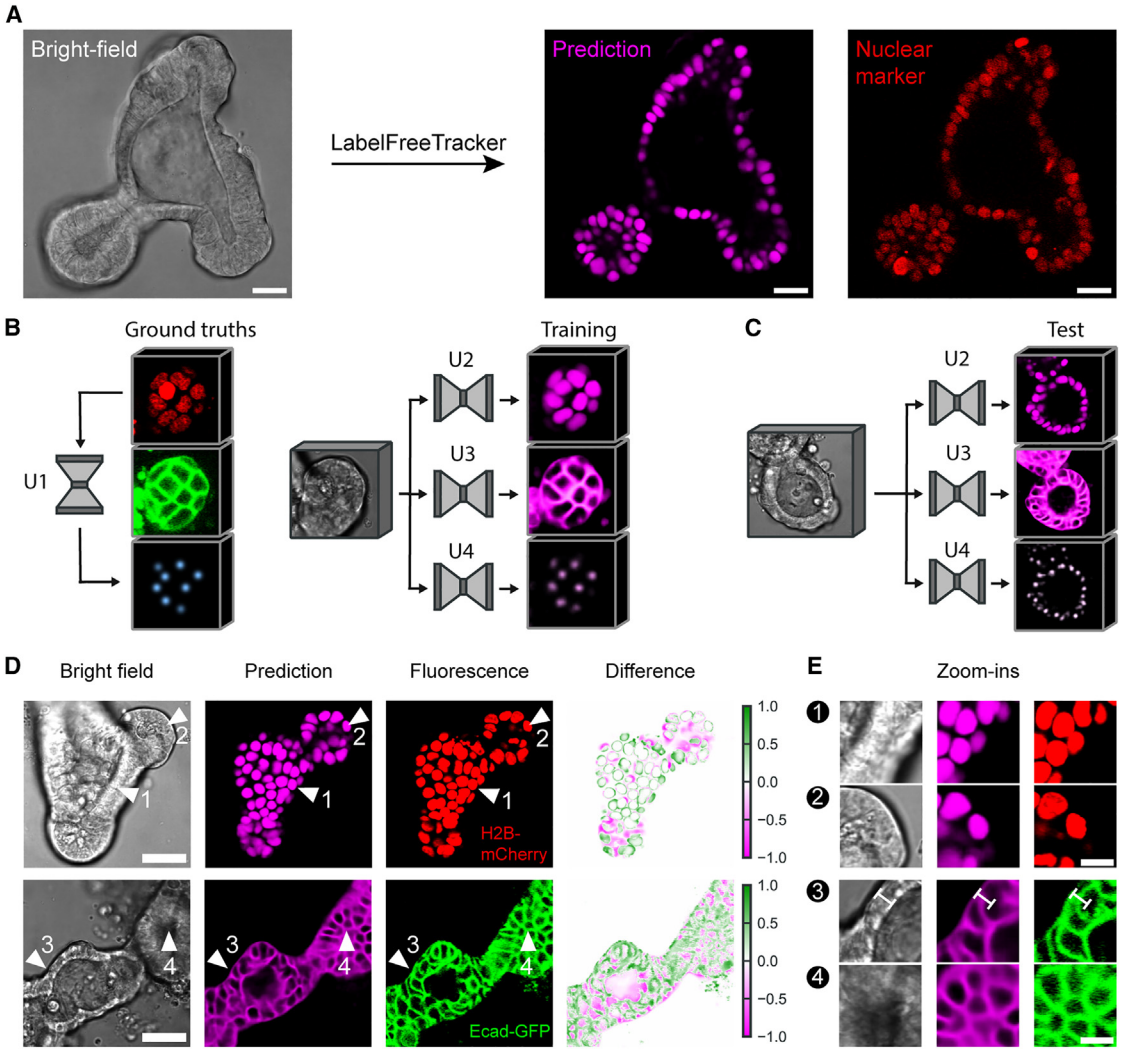


**Figure 1. LabelFreeTracker predicts cell nuclei and membranes from bright-field images of 3D intestinal organoids**

(A) Bright-field image of a mouse intestinal organoid (left), predicted nuclear fluorescence signal by LabelFreeTracker (middle), and measured fluorescence signal (right). Scale bars indicate 20 μm.

(B and C) Overview of the training (B) and testing (C) neural networks that constitute LabelFreeTracker. U1 is used to predict nuclear center positions from nuclear fluorescence images and serves as a ground truth for U4. U2, U3, and U4 are networks trained to predict the nuclear fluorescence, membrane fluorescence, and nuclear center positions from bright-field images, respectively. Micrographs are 128 × 128 pixels, equivalent to 40 × 40 μm.

(D) 2D slices from organoids with the H2B-mCherry nuclear reporter (top) and E-cadherin-GFP reporter (bottom). The difference image shows the difference between normalized measured and predicted fluorescence intensities. Green indicates underprediction, and magenta indicates overprediction. Scale bars indicate 30 μm.

(E) Magnifications of regions indicated by arrowheads in (D). Note that LabelFreeTracker shows correct predictions despite (1) almost no visible nuclear features and edge distortions in villi, (2) some membrane but limited nuclear features in crypts, (3) distortions in the bright-field images suggesting thinner epithelial thickness than found in the measured fluorescence image, and (4) limited membrane features. Scale bars in magnifications indicate 10 μm.

which were all obtained using standard 3D confocal microscopy (80%/20% training/validation split; see training data for nucleus and membrane predictions for details). With this dataset, we trained four different neural networks, each with a 3D U-Net architecture[21,22] (Figure 1B). We first trained a U-Net (U1) to predict nuclear center positions from nuclear fluorescence images acquired with a confocal microscope. This allowed us to obtain a complete ground truth dataset with nuclear fluorescence, membrane fluorescence, nuclear center positions, and the corresponding bright-field images. We then used this complete dataset to train three new neural networks that directly predict the nuclear signal (U2), membrane signal (U3), and nucleus-center points (U4) from the corresponding bright-field images. By training on crypt and villus domains, we included cell types at all positions along the crypt-villus axis and cell shape changes during growth, division, and differentiation. After training, U2, U3, and U4 accurately predicted cell nuclei, membranes, and nuclear positions, respectively, from new bright-field movies

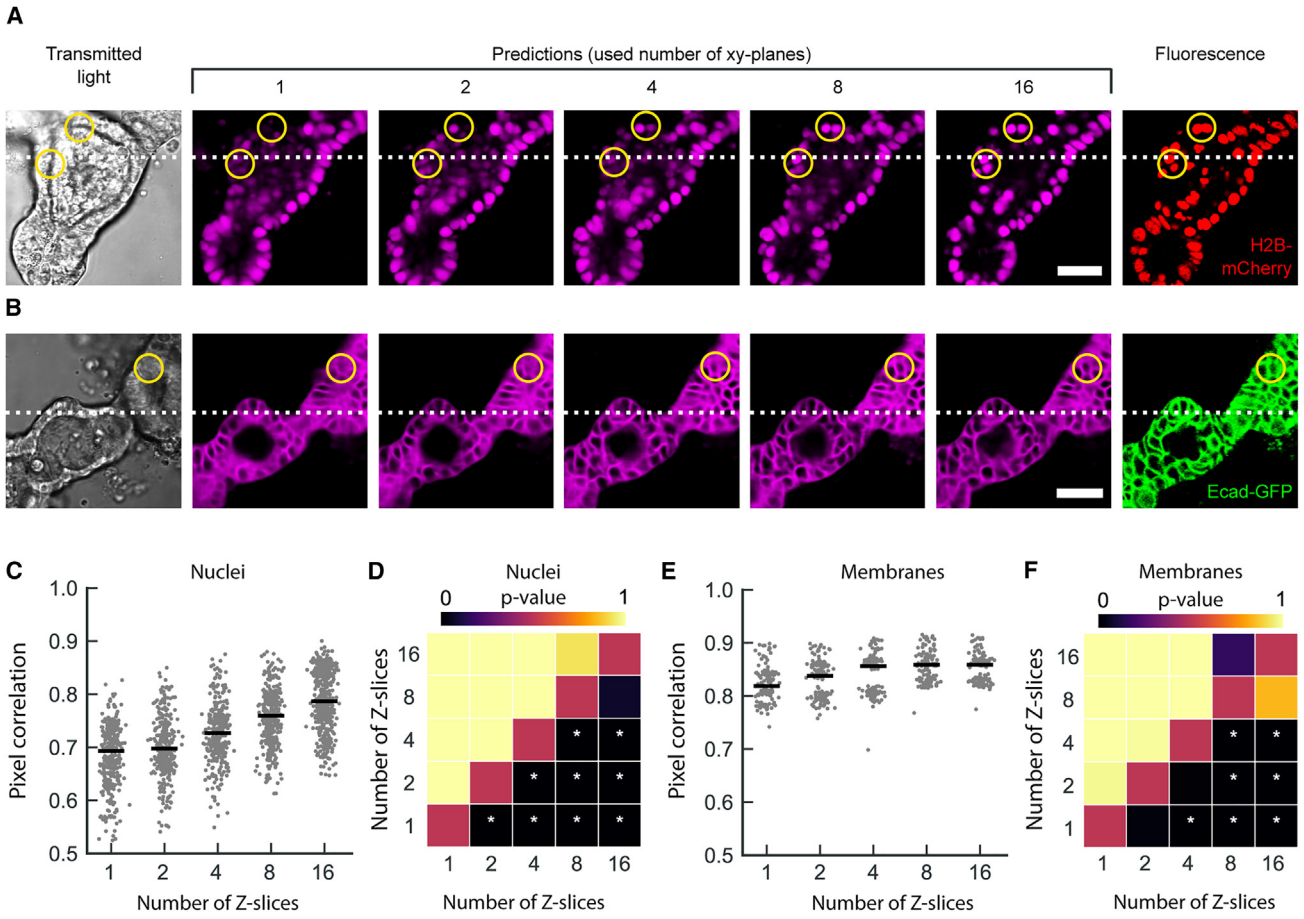


**Figure 2. LabelFreeTracker prediction accuracy increases by combining information across multiple Z slices**

(A) Predictions based on increasing number of Z slices supplied as input to the nucleus prediction network (U2). Yellow circles indicate regions in which a single Z slice predicts poorly but multiple Z slices work well.

(B) Predictions based on increasing number of Z slices supplied as input to the prediction network (U3).

(A and B) Scale bars indicate 30 μm.

(C) Pixel-wise correlations for variants of the nuclear prediction network (U2) with the given number of Z slices (U2). Note that improvements in specific areas (yellow circles in A) are poorly represented in this global metric.

(D) Statistical significance (*p* value) that the number of Z slices on the horizontal axis results in higher correlations than the number of Z slices on the vertical axis (*$p < 0.05$, one-tailed Student's t test).

(E) Pixel-wise correlations for variants of the membrane prediction network (U3) with the given number of Z slices (U3).

(C and E) The horizontal lines indicate the median.

(F) Like (D) but for membranes.

(Figure 1C). LabelFreeTracker identified nuclei and membranes even when these structures were not recognizable by the eye (Figure 1D). Specifically, it correctly predicted the membrane signal in areas where visual inspection of the bright-field images suggested a substantially thinner epithelial layer and, hence, epithelial boundaries at the wrong location (Figure 1D, arrow 3). In some areas, it appeared superior even to the measured fluorescence in recognizing all parts of the membrane, which is key to reconstructing cell shape (Figure S1).

## LabelFreeTracker performance increases with the provided number of Z slices

The ability of LabelFreeTracker to combine information in 3D from many Z slices is important for its identification capabilities. In contrast to the human eye, neural networks can combine information from multiple Z slices in 3D images. To further optimize the prediction process, we assessed the degree to which prediction of fluorescent signals improved with the number of Z slices given to the neural networks. Importantly, we observed strong local differences: In some regions within the imaged volume, LabelFreeTracker was completely unable to identify nuclei and membranes when using a single bright-field Z slice (Figures 2A and 2B, yellow circles). These challenging regions could be properly resolved only when making use of multiple Z slices (Figures 2A and 2B, yellow circles). To further quantify the performance of the U2 and U3 networks, we computed the Pearson correlation coefficient for each pair of measured and predicted fluorescence images (Equation 1):

$$r = \frac{\sum_i (x_i - \bar{x})(y_i - \bar{y})}{\sqrt{\sum_i (x_i - \bar{x})^2 \sum_i (y_i - \bar{y})^2}}. \quad \text{(Equation 1)}$$

Here, $x$ is the fluorescence image, $y$ is the predicted image, $x_i$ and $y_i$ are the intensities in the image at pixel $i$, $\bar{x}$, and $\bar{y}$ are the mean intensities of each entire image. For both nuclear and membrane fluorescent signals, we found that the correlation coefficients increased with an increasing number of Z slices, although the difference between 8 and 16 Z slices was not statistically significant (Figures 2C–2F). We also noted that the minimal values of the correlations increased as more Z slices were used (Figures 2C and 2E).

## Verification and validation of LabelFreeTracker

Overall, LabelFreeTracker identified features over 40 μm into the organoid tissue, enabling full 3D reconstruction of crypt and villus domains (Figure 3A). The percentage of identified nuclei was high up to an imaging depth of 50 μm, after which the performance dropped, with the F1 score showing a similar trend (Figures 3B and S1). To verify that predicted intensity values matched the fluorescence intensity values, we compared the average intensity values in 8 × 8 pixel areas in the predicted and measured fluorescent signals and found close agreement (Figures 3C, S2A, and S2B). Similarly, we computed the Pearson correlation coefficient for the measured and predicted intensity values for individual pixels and found strong correlations for both the nucleus and membranes (0.76 and 0.85, respectively).

Next, we set out to measure how well the predicted foreground (nuclei or membranes) colocalized with the actual foreground. Every pixel reaching at least 10% of the maximum brightness was considered foreground. The intersection-over-union ratios were 0.59 and 0.79 for nuclei and cell membranes, respectively, indicating that the approximation was moderate for nuclear shape and good for cell shape. Within the foreground, the Pearson correlation coefficients were 0.52 and 0.45 for nuclei and membranes, respectively, indicating a moderate correlation between fluorescence intensity and predicted signal. In addition, we analyzed the batch-to-batch variability and found a coefficient of variation of 0.04 and 0.24 for nuclei and membranes, respectively (Figures S2C and S2D).

We also performed a validation experiment to exclude that the presence of fluorescent markers had any detectable effect on the transmitted light signal. To this end, we acquired bright-field images of completely label-free wild-type (WT) organoids and predicted the nuclear signal. Directly after this initial round of imaging, we added a fluorescent dye marking the cell nucleus (Hoechst) and imaged the same organoids after 20 min. In these 20 min, changes in the number of cells were negligible (Figure 3D). We compared the predicted number of cells to the number of cells determined by manual annotation after staining and consistently found a strong correlation (Figure 3E). Furthermore, we computed the convex hull volume of the organoids and the distance between cell centers in the predicted images and found close agreement with the fluorescence images (Figures S2C and S2D).

## Neural-network retraining

To illustrate network retraining for a different experimental setting, we used fluorescent dyes to stain the nucleus (Hoechst) and cell boundaries (EpCam). We acquired time-lapse imaging data consisting of 916 z stack images with accompanying Hoechst and EpCam staining from 91 WT organoids and trained neural networks for nuclear and membrane prediction (Figure 3F). The full process of data acquisition and training took less than 1 day. The resulting network was able to predict nuclei and cell membranes, though, as expected, the results were not as good due the lower-quality staining (Figures 3F–3H). We thus provide a protocol for adapting LabelFreeTracker to other systems and imaging modalities. Note that the training dataset, batch numbers, and training parameters can be adapted to achieve the desired accuracy, depending on the application. This procedure may be further optimized by using more specific and brighter nuclear and membrane dyes and using background correction for images with noticeable background signal.

## Applications of LabelFreeTracker

LabelFreeTracker can be used for quantitative analysis of diverse types of single-cell and organoid analyses. Here, we demonstrate three applications of LabelFreeTracker to illustrate its utility for intestinal organoids. The first application is counting the number of cells in a developing organoid. We used LabelFreeTracker to count the number of nuclei in growing organoids where, at a certain time point, the cell division inhibitors cyclin-dependent kinase 4 and 6 (palbociclib) were added. After addition of palbociclib, the cell count continued to increase for approximately 15 h, after which cell division was effectively blocked (Figure 4A). In contrast, control organoids continued to contain proliferative cells in the same time frame. While methods that quantify the overall organoid size can detect overall changes in organoid growth, they average between cells and, hence, are less suited to address spatially localized proliferation in a small subset of cells. Overall, this assay illustrates how LabelFreeTracker can assess pharmacological interventions on the single cell level without the need for nuclear fluorescent markers.

A second application of LabelFreeTracker is single-cell tracking, which allows lineage tree reconstruction and quantification of fluorescent reporters. Here, we used LabelFreeTracker to analyze live-cell imaging data of an organoid line with a live nuclear reporter for Axin2.[23] *Axin2* is a Wnt target gene that indicates stemness[24] and is only expressed in stem cells at the bottom of the intestinal crypt. We reconstructed lineage trees of individual cells tracked for over 60 h (Figures 4B–4D, Video S1). In these tracks, we measured the fluorescence intensity of the Axin2-sGFP signal for all individual cells. Three types of cells were clearly distinguishable (Figures 4B–4D and S3). First, stem cells were identified that remained in the stem cell zone at the bottom of the crypt. They remained proliferative throughout the duration of imaging and kept high levels of Axin2-sGFP (Figures 4B–4D, red line). The second category was transit-amplifying cells, which remained proliferative but lost their Axin2-sGFP marker as they moved away from the stem cell zone (Figures 4B–4D, blue line). The third category was differentiating cells, which stopped proliferating for over 24 h and had lost all their Axin2-sGFP signal (Figures 4B–4D, green

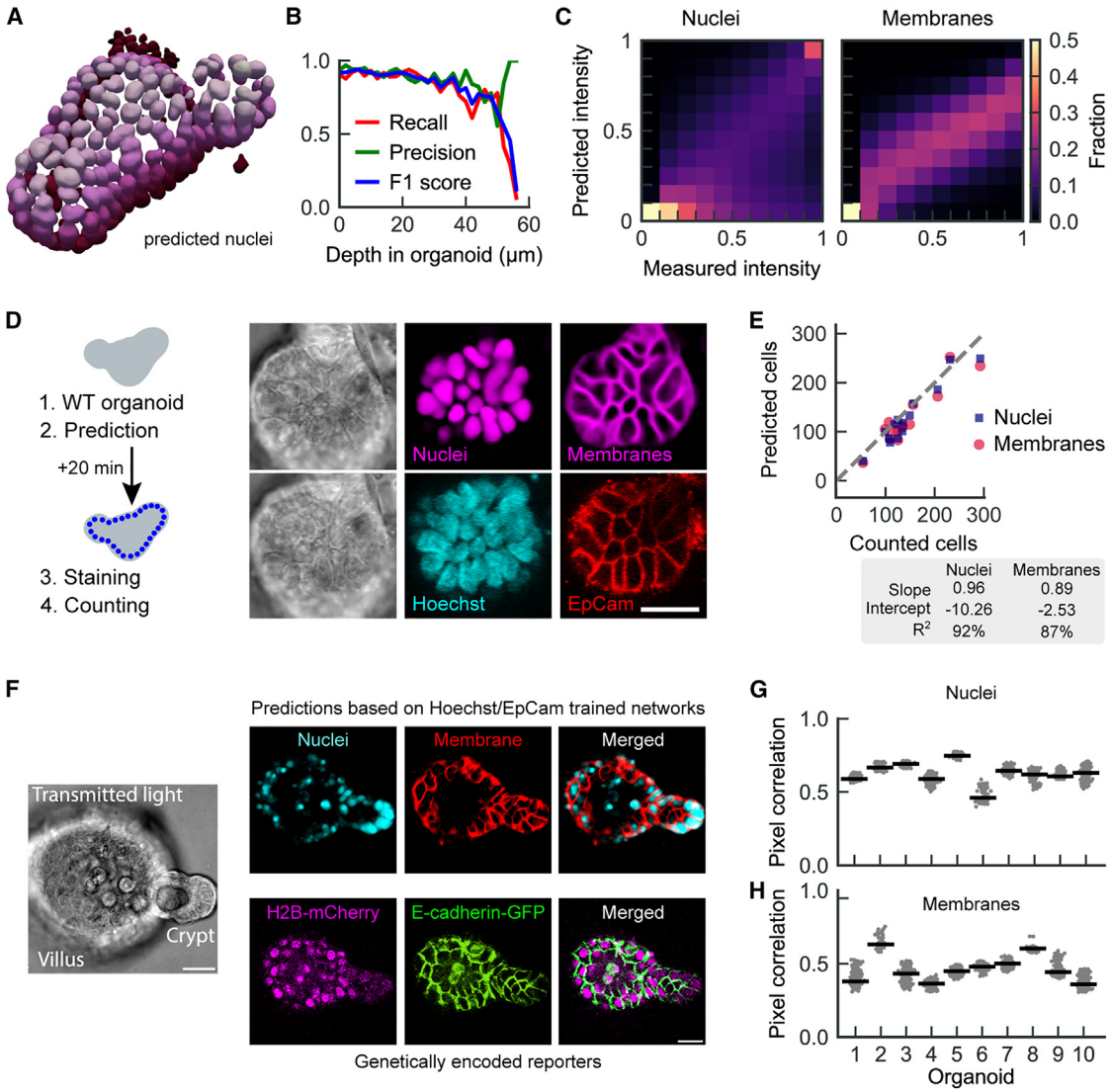


**Figure 3. Verification and validation of LabelFreeTracker**

(A) 3D reconstruction of nuclear predictions up to 50 μm deep into the tissue.

(B) Precision, recall, and F1 score of nuclear prediction against depth ($n$ = 15 stacks from three organoids). The precision is the number of correctly predicted nuclei divided by the total number of predicted nuclei (TPs and FPs together). The recall is the number of correctly predicted nuclei divided by the actual number of nuclei. The F1 score is the harmonic average of the precision and the recall.

(C) Predicted versus measured fluorescence intensity for 8 × 8-pixel areas (327 and 136 stacks for nuclei and membranes, respectively, each from 3 organoids). Fractions were normalized so that the columns add up to 1.

(D) Bright-field image of a WT organoid before staining, with nuclear and membrane prediction (top row), and bright-field image of a WT organoid after staining with Hoechst and a conjugated EpCam antibody (bottom row). The scale bar indicates 20 μm.

(E) Number of cells predicted by the nucleus-center prediction network (blue squares) and membrane network (red dots) versus number counted after subsequent Hoechst staining ($n$ = 14 organoids).

(F–H) LabelFreeTracker retraining for organoids stained for nuclei and membranes with fluorescent dyes (Hoechst and EpCam, respectively).

(F) A bright-field image (left) was used to predict nuclei and membranes using the retrained LabelFreeTracker network (top row). The bottom row shows the genetically encoded reporters H2B-mCherry and E-cadherin-GFP for comparison. Scale bars indicate 20 μm.

(G and H) Pearson correlation coefficients for predicted and measured nuclear (G) and membrane (H) signals using the retrained network. A horizontal line indicates the median Pearson correlation.

line). This shows that LabelFreeTracker allows the reconstruction of lineage trees of individual cells with high linking accuracy (Figure S4) while leaving fluorescence channels available to resolve key developmental processes.

A third application of LabelFreeTracker is the quantification of cell volume over time (Figures 4E–4G). Importantly, this requires cell membrane reconstruction on all sides for many time points, which is especially challenging in dense epithelia. To measure

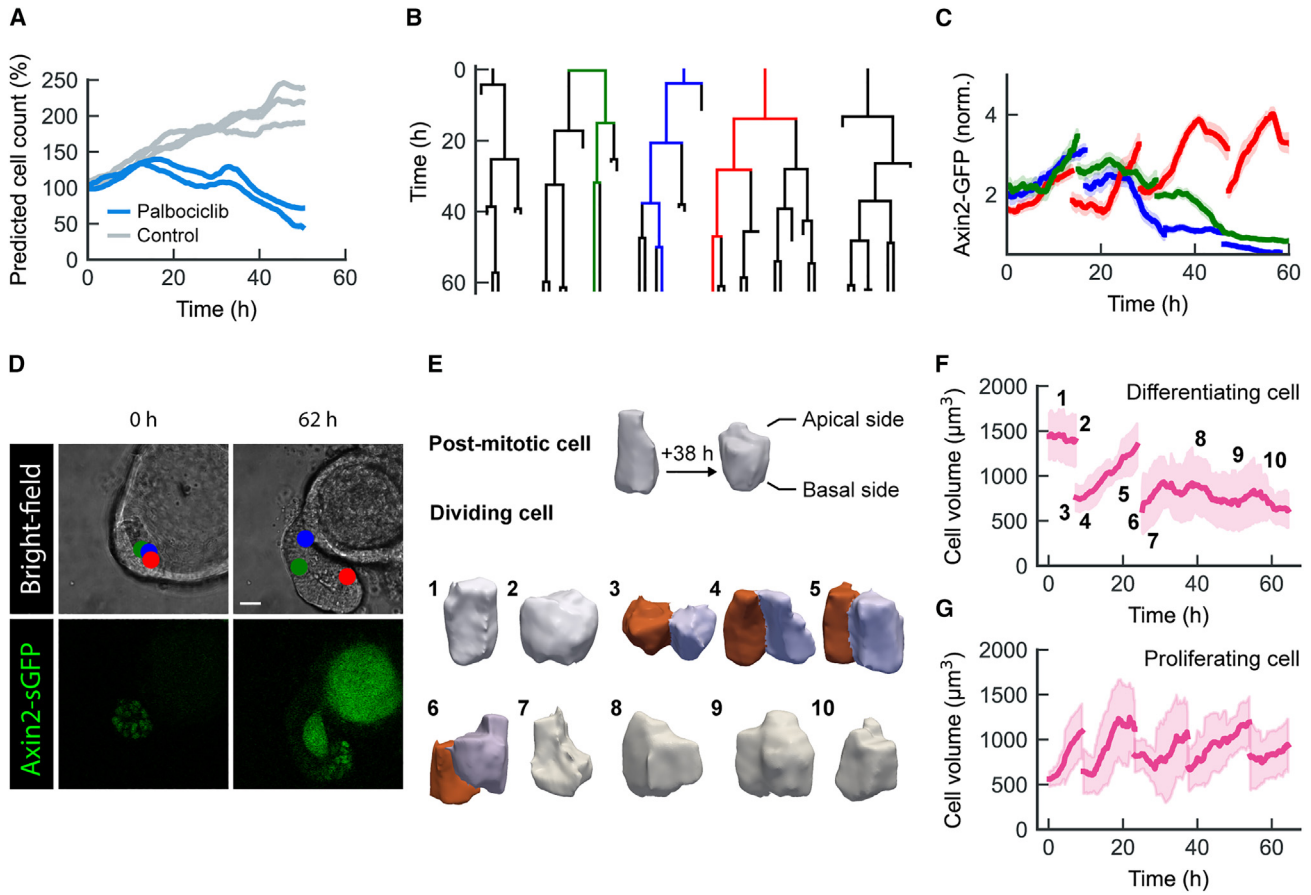


**Figure 4. Applications of LabelFreeTracker**

(A) Predicted cell count in control organoids (gray) and in organoids where cell division is blocked pharmacologically by palbociclib (blue).

(B) Lineage trees of cells in Axin2-sGFP reporter organoids tracked over 60 h. A green lineage indicates a cell that eventually differentiates, whereas the blue and red lineages indicate cells that remain proliferative throughout the time lapse.

(C) Normalized measurements of Axin2-sGFP fluorescent signal for the branches highlighted in (B) (see Methods for details of normalization). The green, blue, and red curves correspond to the cells that are in the villus, transit-amplifying region, and crypt, respectively, at the end of the time lapse. Areas around the lines represent the standard error of an 8-h time window.

(D) Images corresponding to (B), showing the positions of the highlighted cells along the crypt-villus axis at the start (0 h) and end (62 h) of the time lapse. The scale bar indicates 20 μm.

(E) 3D rendering of the predicted volume of a post-mitotic cell (top) and dividing cell (bottom).

(F) Predicted cell volume over time for the mitotic cell in (E).

(G) Predicted volume for a cell that remains proliferative (same organoid as in E and F).

(F and G) Areas around the curves represent the standard deviation of a 6-hour time window.

cell volumes, we segmented the cells using the predicted membrane signal. For each time point, we first predicted the membrane signal of each image. Next, we obtained a mask of the entire organoid by thresholding (10% of the maximum intensity) the predicted membrane signal, closing any holes, and eroding the final mask by four pixels. Using a watershed algorithm with the predicted nucleus-center points as seeds then yields a full 3D reconstruction of individual cells (Figure 4E). Here, we exploited the fact that the predicted signal is smooth, as it lacks imaging noise, thus creating a favorable intensity landscape for the watershed algorithm. While cell volume at individual time points was noisy, a 6-h moving average gave consistent predictions of cell volume over time. The 3D reconstructions during one cell cycle showed cells rounding up during cell division, the formation of a narrow apical surface directly after division and then finally growing again in volume (Figure 4E). Volume growth showed an expected doubling during the cell cycle for dividing lineages but also a notably sudden arrest directly after the last division (Figures 4F and 4G), which correlates with cell differentiation.[5]

## DISCUSSION

With the development of organoid models, highly dynamic processes can be directly observed through live-cell imaging in a broad range of tissues. Live-cell microscopy, however, comes with a set of limitations, such as the limited number of fluorescent labels due to spectral overlap, phototoxicity, photobleaching, and laborious manual data annotation.[25] To overcome these

limitations, label-free imaging approaches present an exciting direction. Previously, label-free or *in silico* labeling methods have been developed,[17–19] but they were only used to predict cellular structures in bright-field 3D z stacks of flat, 2D monolayer cell cultures, which are not hampered by light scattering of intervening tissue. Additionally, a recent study presented a method to predict the nuclei of cells in spheroids inside a microfluidic chip for high-content screening applications.[26] To broaden the scope of label-free imaging to 3D organoid cultures, we developed LabelFreeTracker, a machine-learning based algorithm for the prediction of nuclei, membranes in 3D, as well as their tracking through time. LabelFreeTracker is based on 4 U-Net neural networks that together predict nuclear and membrane fluorescence and nucleus-center positions from bright-field images as obtained from the transmitted light in standard confocal microscopy. Strikingly, LabelFreeTracker accurately predicted the cell nuclei and membranes even in cases where these structures were completely invisible to the human eye (Figure 1A). To some extent, this can be explained by the fact that, in contrast to the human eye, LabelFreeTracker is able to simultaneously integrate information from multiple slices of a 3D stack. LabelFreeTracker allows reconstruction of nuclear volumes up to 50 μm deep into the tissue, after which recall (that is, the percentage of retrieved nuclear center positions) drops sharply. We demonstrated the applicability of LabelFreeTracker with three use cases of tracking the dynamics of individual cells over longer periods of time, though it can also be used for static analysis at a single time point. First, we showed that LabelFreeTracker can perform cell counting in organoids grown under normal conditions and conditions where cell division was pharmacologically blocked. Second, we demonstrated that it enables cell tracking and, hence, allows complete lineage tree reconstructions and quantification of intracellular fluorescent signal from transcriptional reporters. Finally, we showed that our approach allows quantification of the dynamics of single-cell shape and volume.

LabelFreeTracker is especially promising as a tool for quantitative analysis of dynamic processes in patient-derived organoids. For example, our approach allows automated tracking of cells across multiple divisions and therefore makes it possible to directly test the effect of drugs and pharmacological treatments that target cell proliferation. While we focused on the prediction of nuclei and membranes of mouse intestinal organoids, LabelFreeTracker can be readily expanded to other organoid systems. Extending LabelFreeTracker to other organoid systems and/or imaging setups requires training datasets of bright-field images paired with nuclear/membrane fluorescence images. Key here are the size of the training dataset, the imaging resolution in space and time, and the laser power. While the desired reconstruction quality can differ between applications, we note these guidelines (see methods for specific numbers): (1) The size and diversity of the training dataset should be such that all organoid morphologies are represented and that different batches are included. (2) For tracking cells across multiple generations, the time resolution should be such that at least two images are taken during each cell division. This ensures that two daughter cells can be connected to the corresponding mother cell. (3) The Z resolution should be set so that nuclei span multiple (3 or more) Z slices. In the case of mouse intestinal organoids, we found that this criterion was satisfied for 2-μm intervals between Z slices. (4) Bright-field images must not be over- or undersaturated, as this dramatically affects the training and performance (Figure S5). Finally, while we have here only shown that LabelFreeTracker works for nuclei and membranes, the approach may be extended to identify other subcellular features, such as mucin in goblet cells, nucleoli, microtubules, and mitochondria.[17]

## METHODS

### Organoid culturing

Organoids were cultured under standard conditions in ENR medium.[27] Briefly, organoids were seeded in gel consisting of basement membrane extract (BME2, Trevingen) mixed with Advanced DMEM/F-12 at a 2:1 to 3:1 volume ratio. This medium consisted of Advanced DMEM/F-12 (Life Technologies) with the following added ingredients: murine recombinant epidermal growth factor (50 ng/mL, Life Technologies), murine recombinant Noggin (100 ng/mL, PeproTech), human recombinant R-spondin 1 (500 ng/mL, PeproTech), *N*-acetylcysteine (1 mM, Sigma-Aldrich), N2 supplement (1×, Life Technologies), B27 supplement (1×, Life Technologies), GlutaMAX (2 mM, Life Technologies), HEPES (10 mM, Life Technologies), and penicillin/streptomycin (100 U/mL, Life Technologies).

The organoids were passaged every week, after which they were re-fed twice during the next 7 days. The passaging was carried out as follows. The organoids from two wells were collected in Advanced DMEM/F-12 medium and mechanically disrupted by pipetting up and down with a narrowed glass pipette. Subsequently, the organoids were spinned down for 5 min at 320 g. Supernatant was aspirated and a second centrifugation round was carried out. The supernatant was again removed, and then the organoids were seeded in gel on wells of a new culture plate. After leaving the plates in an incubator for 20–30 min, the growth medium was added.

### Organoid lines

H2B-mCherry/Lgr5-GFP and WT murine intestinal organoids were a gift from Norman Sachs and Joep Beumer (Hubrecht Institute, the Netherlands). H2B-mCherry/E-cadherin-GFP organoids were a gift from Daniel Krueger (Hubrecht Institute, the Netherlands). $Axin2^{P2A\text{-}rtTA3\text{-}T2A\text{-}3\times NLS\text{-}SGFP2}$; tetO-Cre; $Rosa26^{mTmG}$ murine intestinal organoids were a gift from the Van Amerongen lab (Universiteit van Amsterdam, the Netherlands).[27]

### Organoid time-lapse microscopy

One or two days before the start of the time lapse experiment, we seeded mechanically dissociated organoids in BME2 gel in four-well chambered cover glass (CellVis), using the same procedure as during passaging. To prevent the gel from solidifying immediately, seeding was performed on a cold block. The imaging well was put at 4°C for 10 min to allow the organoids to sediment down. Afterward, the chambered cover glass was put at 37°C and 5% $CO_2$ to allow the gel to solidify. After leaving the plates in an incubator for 20–30 min, the growth medium was added. Imaging was performed on a Nikon A1R MP microscope with a 40× oil immersion objective (NA = 1.30). 31 Z slices with

2 μm step size were taken per organoid every 12 min. Experiments were performed at 37°C and 5%–8% $CO_2$, achieved by using a stage-top incubator (Okolab). An imaging well typically contains over 50 organoids, of which we imaged about 20 per experiment. We selected for a diverse set of organoids, as our goal was to obtain a diverse training set. By diverse, we mean that organoids had different sizes, number of crypts, morphologies (cystic, bulged, budded, etc.), and degrees of debris present in and around the organoid. We set the imaging settings so that the bright field was never oversaturated or undersaturated. For the fluorescent channels for imaging H2B and E-cadherin, we aimed to make all cells anywhere in the imaged part of the organoid appear as bright cells at the cost of oversaturation elsewhere in the organoid.

### Imaging and measuring Axin2 reporter organoids

The organoids were passaged 1 day before the experiment and imaged over an entire weekend as described above. We performed semiautomatic tracking on these organoids (see above) and corrected the tracks for five larger lineage trees. We then segmented all cells at all time points (see above) and used the obtained masks to measure the total Axin2-sGFP2 signal of every cell. We noticed that a specific type of cell segmentation error was causing issues with the sGFP2 measurement. Sometimes, the membranes between two cells were missing, likely because the neural network could not locate it. This caused the volume of one cell to be assigned to a neighbor of the cell. This error was largely eliminated by averaging the predicted membranes with a distance map, which was 0 at the center of the cell and then increased linearly up to 1 at a distance of 7 μm. In this average, the membranes had a weight of 75% and the distance map a weight of 25%. The downside of adding the distance map to the watershed landscape is that, for cells that are both large and stretched, it causes them to appear more spherical than they are. For measuring the intensity of a nucleus-localized signal, this is not an issue, but for measuring the volume of the cell it is. Therefore, we only used the distance map for measuring Axin2-sGFP2 and not for measuring the cell volume. The Axin2-sGFP2 signals were then normalized as follows. The lowest measured Axin2-sGFP2 signal in the time lapse was assumed to correspond to the background. This background, measured in intensity per pixel, was then subtracted from every measured Axin2-sGFP2 signal. The intensities were then multiplied by a factor so that the median intensity of the organoid, across all time points, was 1. To reduce noise in the measured Axin2 signal, we applied a moving average with an 8-h time window.

### Inhibition of cell division

A 5.6 mM palbociclib (Sigma-Aldrich) stock solution was prepared by dissolution in endotoxin-free demineralized water. A few hours before the start of a time-lapse movie, a certain amount of the thawed stock solution was added to the medium so that the final concentration in the medium was 10 μM.

### Training data for nucleus and membrane predictions

For acquiring training data of nuclear fluorescence, we used H2B-mCherry/Lgr5-GFP murine intestinal organoids, which were a gift from Norman Sachs and Joep Beumer (Hubrecht Institute, the Netherlands). For acquiring training data of membrane fluorescence, we used H2B-mCherry/E-cadherin-GFP organoids, which were a gift from Daniel Krueger (Hubrecht Institute, the Netherlands). We did not use this line to create nucleus prediction training data, as the nuclear marker of this line is less bright compared to our other line. We used E-cadherin as a membrane marker even though it technically only marks cell-cell junctions. In practice, this is not a problem, as the intestinal epithelium is a tightly connected epithelium. As a result, often the entire cell surface is still visible in images of E-cadherin. We used this fluorescence marker because it produced a bright signal in our organoids, making it easy to image. We collected 3,894 paired images of bright-field/nuclei, which consisted of 22 organoids in total. 13 organoids were newly imaged, and the rest were from a previous publication.[9] The data consist of four independent experiments. In addition, we collected 1,908 paired images of bright-field/membranes of 25 organoids distributed over two independent experiments. The images were split into a training/validation set using an 80%/20% split at the individual time point level. The same organoid can thus appear in both the training and validation sets, although always at different time points. We normalized the time lapse so that, at all time points and all depth layers, the fluorescent signal was saturated. Different normalizations were sometimes used for different depths and time points. We split the 512 × 512 × 32 pixel images in smaller patches of 128 × 128 × 16 pixels. For many of our images, the organoids did not occupy the entire view, which caused a considerable number of patches to show no fluorescence. To speed up the training process, we removed almost all of these patches. A patch was considered black if the brightest pixel found in the patch was lower than half of the highest fluorescence in the entire image. We kept 5% of the black patches in the training set so that the network still learned to not predict any fluorescence outside the organoid. We first trained the network that predicted the nuclear signal from the bright field and then the network that predicted the membrane signal. For the network predicting the membrane signal, we used the trained network that predicted nuclei as a starting point so that the cell membrane network could reuse cell detection knowledge of the nuclear network. We trained the network to minimize the mean squared error loss between the fluorescent signal and the predicted signal.

### Testing data for nucleus and membrane predictions

For the testing data in Figures 2 and 3A–3C, we used an additional 4 organoids (same line) for the nucleus network (544 image pairs). Three organoids were from a previous publication.[9] For testing the membrane predictions, we imaged 2 organoids in 2 independent experiments (136 image pairs). The microscope, imaging settings/conditions, and organoid lines were identical to those for the training data.

### Predicting nucleus-center positions

For training the nucleus-center position network, we used pairs of bright-field images and images with bright spots at the center of the nuclei. We first used OrganoidTracker[9] to automatically find the nucleus centers in our training set, based on the

fluorescent nuclei. Then, we created images with bright Gaussian spots at the location of the nucleus centers with the standard deviations of the Gaussian function $\sigma_x$ and $\sigma_y$ being 4 pixels (1.28 μm), and $\sigma_z$ being 1 pixels (equal to 2 μm in this case, as the resolution is lower in the z direction). We trained the neural network on the training set for 10 epochs. A large part of the images containing the nucleus centers was black, as there were no nucleus centers within a few pixels. Therefore, the network tended to just predict all pixels as black and not draw any nucleus centers at all. We solved this issue by reducing the weight of black pixels by a factor of 4. To test the network, we applied the network to three organoids. We first obtained a ground truth for five time points in each of these organoids by manually annotating all cell centers at these time points. We selected the time points at 0%, 25%, 50%, 75%, and 100% of the time lapse duration. To obtain a performance metric, we used the following method to calculate the number of true positives (TPs), false positives (FPs), and false negatives (FNs). Any nucleus center detected by the neural network was assigned to the closest nucleus center from the ground truth under the condition that the distance was no longer than 5 μm. Every nucleus center cannot have more than one assignment. Each successful assignment was a TP. Then, any manually tracked nucleus center that was left with no assignments became an FN. Finally, any nucleus center from the neural network that was left with no assignments was regarded as an FP. The precision was then calculated as $TP/(TP + FP)$, and the recall was calculated as $TP/(TP + FN)$. The $F_1$ score is the harmonic average of the precision and recall: $F_1 = 2 \cdot (\text{precision} \cdot \text{recall})/(\text{precision} + \text{recall})$.

## Prediction neural network

The network architecture follows a U-Net type architecture with a downward block, an upward block, and skip connections between the blocks. The input of the network consists of 3D grayscale images of 128 × 128 × 16 pixels. The downward part of the network consists of four repeating units, with each unit consisting of 2 3D convolutions, maximum pooling, and batch normalization. The upward part consists of four repeating units, with each unit consisting of a transposed convolution, followed by two convolutions, followed by batch normalization. At the end of the network, a final convolution is done. The network is optimized using the Adam optimizer[28] with the mean squared error loss function. The intensities of the bright-field images are offset and multiplied so that the average of an entire 3D stack of a single time point is 0, and the standard deviation is 1. For the fluorescence images, the images were normalized from 0 to 1 with the background at 0. Normalization factors were chosen by hand for several slices during the time lapse at different times and depths. For other slices, the factors were calculated from the manually set factors by linear interpolation. The only data augmentation that was done was horizontal and vertical flipping. Rotations and scaling data augmentations were omitted on purpose to not remove any details provided by individual pixels.

## Comparison of human annotated and predicted cell counts in WT organoids

To demonstrate that bright-field-based prediction of nuclei works in label-free organoids, WT mouse intestinal organoids were mechanically disrupted and embedded in BME2 gel with growth medium. Two days after passaging, z stacks of label-free organoids were acquired. After the first image acquisition, cells were incubated for 15–25 min in live-cell staining medium consisting of growth medium supplemented with Hoechst 34580 and 0.8 μg/mL Alexa 647-conjugated anti-mouse CD326 antibody (Invitrogen, 17-5791-80) before a second z stack was acquired with the same imaging conditions as for the label-free image acquisition. In each organoid, the centers of all nuclei were manually annotated based on the Hoechst signal, and the centers of all nuclei were automatically predicted by an independent human annotator using the LabelFreeTracker algorithm. This last annotator also manually annotated all cell centers based on the predicted membrane signal.

## Semiautomated cell tracking

We used the position detection network (see predicting nucleus-center positions) to generate a set of positions. Our next step was to link these positions over time. As a first step, we estimated the chance $P(L|d)$, which is the chance of two cell positions in subsequent time points being of the same cell (i.e., having a link L), given the distance d between both positions. This function is expected to start at a high chance for $d = 0$ and then drop off toward 0 for increasing d. To estimate this function, we used the tracking data of one organoid with a nuclear marker that was tracked previously.[9] For every position, we recorded the distance to the nearest position at the previous time point as well as the distance to any position that is at most twice as far. We also recorded whether that position represented the same cell, which allowed us to estimate the chance $P(L|d)$. We noticed that the center positions of the predicted nuclei were less accurate than the center positions of fluorescent nuclei. This resulted in larger apparent cell movements in between time points, which made the function $P(L|d)$ underestimate the chance of two nucleus positions being of the same cell. To correct for this, we simulated errors in the nucleus-center positions of our previously tracked organoid. We added $(\text{rand}() - \text{rand}()) \cdot 1.6$ μm to the x and to the y coordinate of each position, with rand() a function that returns a uniformly distributed random number from 0 to 1. For the z coordinate, we choose a random integer from 1 to 6 (inclusive); if the number was 5, then we added 2 μm (corresponding to one z layer) to the z coordinate, and if the number was 6, then we subtracted 2 μm.

Having obtained a representation for $P(L|d)$, we used this as input for the track creation algorithm of Haubold et al.[29] This algorithm presents an approximate solution of the problem of linking cell detections over time. It builds on the shortest path min-cost flow-solving algorithm but adapts the residual graph so that divisions become possible. Although the algorithm cannot guarantee an optimal solution, a good performance is nonetheless achieved within polynomial time. Besides the linking probabilities described in the previous paragraph, the algorithm additionally expects probabilities of a cell to divide at a given time point as input. We provided those with a single baseline division probability. As a result, the solver could only detect a few divisions (<5 divisions per organoid). Using OrganoidTracker,[9] we

manually corrected these tracks for five lineages, thereby adding the missing cell divisions.

### Comparison of cell linking performance

Cell linking performance was compared against manual tracking based on a fluorescent nuclear marker. The same set of testing organoids was used as for validating nucleus and membrane prediction performance. We manually tracked part of each organoid. We then performed automatic tracking as described in the previous section and then used the links comparison feature of OrganoidTracker[9] to calculate the recall, precision, and F1 score. The comparison was done by matching manually annotated nucleus centers to automatically detected nucleus centers close by, up to a distance of 5 μm, and then checking whether the links of the position match. Areas where no manual center annotations were created (i.e., where automatically detected center positions could not be matched to any manual annotation close by) were excluded from the performance evaluation.

### Reconstruction of cell shape in organoids

Here, we used a time-lapse movie of the H2B-mCherry/Lgr5-GFP organoids, where the Lgr5-GFP channel was not imaged. A membrane signal was predicted for each time point as well as nucleus-center points, both based on the transmitted light image of the confocal microscope. This signal was first used to reconstruct a mask of the entire organoid; the predicted membrane signal was thresholded at 10% of the maximum signal, followed by closing any holes in the mask and eroding the final mask by four pixels. Next, we reconstructed the masks of single cells using a 3D watershed algorithm (Mahotas[30]) with the predicted nucleus-center points as seeds and the predicted membrane signal as the watershed landscape. The measured volume over time was noisy for most cells; to correct for this, a 6-h moving average window was applied.

### Software packages

The panels follow the standard boxplot settings of the software library Matplotlib[31] version 3.6.0. Neural networks were implemented in Tensorflow[32] version 2.5.1. The 3D watershed algorithm was provided by the Mahotas[30] software library.

## RESOURCE AVAILABILITY

### Lead contact

Requests for further information, resources, and reagents should be directed to and will be fulfilled by the lead contact, Sander J. Tans (s.tans@amolf.nl).

### Materials availability

This study did not generate new unique reagents or organoid lines.

### Data and code availability

- The raw imaging data reported in this study cannot be deposited in a public repository due to its size. To request access, contact the lead contact.
- All original code has been deposited at Zenodo (Zenodo: https://doi.org/10.5281/zenodo.14814672)[33] and is publicly available.
- Any additional information required to reanalyze the data reported in this paper is available from the lead contact upon request.

## ACKNOWLEDGMENTS

We thank Xuan Zheng and Guizela Huelsz-Prince for contributing raw data to the training dataset. We thank Daniel Krueger, Renée van Amerongen, Joep Beumer, and Norman Sachs for kindly sharing organoid lines with us. We also thank all members of the Sander Tans and Jeroen van Zon groups for fruitful discussions of this work. This work was funded by the NWO Building Blocks of Life grant from the Dutch Research Council (737.016.009 to R.N.U.K, J.S.v.Z., and S.J.T.) and the NWO Groot grant from the Dutch Research Council (2019.085 to W.K.S., M.A.B., J.S.v.Z., and S.J.T.).

## AUTHOR CONTRIBUTIONS

Conceptualization, R.N.U.K., W.K.S., J.S.v.Z., and S.J.T; methodology, R.N.U.K., W.K.S., and M.A.B.; investigation, R.N.U.K., W.K.S., and M.A.B.; writing – original draft, R.N.U.K. and W.K.S.; writing – review & editing, all authors; funding acquisition, J.S.v.Z. and S.J.T; supervision, J.S.v.Z. and S.J.T.

## DECLARATION OF INTERESTS

The authors declare no competing interests.

## DECLARATION OF GENERATIVE AI AND AI-ASSISTED TECHNOLOGIES

No generative AI or AI-assisted technologies were used in this work.

## SUPPLEMENTAL INFORMATION

Supplemental information can be found online at https://doi.org/10.1016/j.xcrp.2025.102522.

Received: March 26, 2024
Revised: February 19, 2025
Accepted: March 12, 2025
Published: April 7, 2025

## REFERENCES

1. Clevers, H. (2016). Modeling Development and Disease with Organoids. Cell *165*, 1586–1597. https://doi.org/10.1016/j.cell.2016.05.082.
2. De Medeiros, G., Ortiz, R., Strnad, P., Boni, A., Moos, F., Repina, N., Challet Meylan, L., Maurer, F., and Liberali, P. (2022). Multiscale light-sheet organoid imaging framework. Nat. Commun. *13*, 4864. https://doi.org/10.1038/s41467-022-32465-z.
3. Huelsz-Prince, G., Kok, R.N.U., Goos, Y., Bruens, L., Zheng, X., Ellenbroek, S., Van Rheenen, J., Tans, S., and van Zon, J.S. (2022). Mother cells control daughter cell proliferation in intestinal organoids to minimize proliferation fluctuations. Elife *11*, e80682. https://doi.org/10.7554/eLife.80682.
4. Randriamanantsoa, S., Papargyriou, A., Maurer, H.C., Peschke, K., Schuster, M., Zecchin, G., Steiger, K., Öllinger, R., Saur, D., Scheel, C., et al. (2022). Spatiotemporal dynamics of self-organized branching in pancreas-derived organoids. Nat. Commun. *13*, 5219. https://doi.org/10.1038/s41467-022-32806-y.
5. Zheng, X., Betjes, M.A., Ender, P., Goos, Y.J., Huelsz-Prince, G., Clevers, H., Van Zon, J.S., and Tans, S.J. (2023). Organoid cell fate dynamics in space and time. Sci. Adv. *9*, eadd6480. https://doi.org/10.1126/sciadv.add6480.
6. Betjes, M.A., Zheng, X., Kok, R.N.U., Van Zon, J.S., and Tans, S.J. (2021). Cell Tracking for Organoids: Lessons From Developmental Biology. Front. Cell Dev. Biol. *9*, 675013. https://doi.org/10.3389/fcell.2021.675013.
7. Sugawara, K., Çevrim, Ç., and Averof, M. (2022). Tracking cell lineages in 3D by incremental deep learning. Elife *11*, e69380. https://doi.org/10.7554/eLife.69380.

8. Ulicna, K., Vallardi, G., Charras, G., and Lowe, A.R. (2021). Automated Deep Lineage Tree Analysis Using a Bayesian Single Cell Tracking Approach. Front. Comput. Sci. *3*, 734559. https://doi.org/10.3389/fcomp.2021.734559.

9. Kok, R.N.U., Hebert, L., Huelsz-Prince, G., Goos, Y.J., Zheng, X., Bozek, K., Stephens, G.J., Tans, S.J., and van Zon, J.S. (2020). OrganoidTracker: Efficient cell tracking using machine learning and manual error correction. PLoS One *15*, e0240802. https://doi.org/10.1371/journal.pone.0240802.

10. Keshara, R., Kim, Y.H., and Grapin-Botton, A. (2022). Organoid Imaging: Seeing Development and Function. Annu. Rev. Cell Dev. Biol. *38*, 447–466. https://doi.org/10.1146/annurev-cellbio-120320-035146.

11. Xue, Y., Browne, A.W., Tang, W.C., Delgado, J., McLelland, B.T., Nistor, G., Chen, J.T., Chew, K., Lee, N., Keirstead, H.S., and Seiler, M.J. (2021). Retinal Organoids Long-Term Functional Characterization Using Two-Photon Fluorescence Lifetime and Hyperspectral Microscopy. Front. Cell. Neurosci. *15*, 796903. https://doi.org/10.3389/fncel.2021.796903.

12. Borten, M.A., Bajikar, S.S., Sasaki, N., Clevers, H., and Janes, K.A. (2018). Automated brightfield morphometry of 3D organoid populations by OrganoSeg. Sci. Rep. *8*, 5319. https://doi.org/10.1038/s41598-017-18815-8.

13. Deben, C., De La Hoz, E.C., Compte, M.L., Van Schil, P., Hendriks, J.M.H., Lauwers, P., Yogeswaran, S.K., Lardon, F., Pauwels, P., Van Laere, S., et al. (2023). OrBITS: label-free and time-lapse monitoring of patient derived organoids for advanced drug screening. Cell. Oncol. *46*, 299–314. https://doi.org/10.1007/s13402-022-00750-0.

14. Haja, A., Horcas-Nieto, J.M., Bakker, B.M., and Schomaker, L. (2023). Towards automatization of organoid analysis: A deep learning approach to localize and quantify organoid images. Comput. Methods Programs Biomed. Update *3*, 100101. https://doi.org/10.1016/j.cmpbup.2023.100101.

15. Montes-Olivas, S., Legge, D., Lund, A., Fletcher, A.G., Williams, A.C., Marucci, L., and Homer, M. (2023). In-silico and in-vitro morphometric analysis of intestinal organoids. PLoS Comput. Biol. *19*, e1011386. https://doi.org/10.1371/journal.pcbi.1011386.

16. Matthews, J.M., Schuster, B., Kashaf, S.S., Liu, P., Ben-Yishay, R., Ishay-Ronen, D., Izumchenko, E., Shen, L., Weber, C.R., Bielski, M., et al. (2022). OrganoID: A versatile deep learning platform for tracking and analysis of single-organoid dynamics. PLoS Comput. Biol. *18*, e1010584. https://doi.org/10.1371/journal.pcbi.1010584.

17. Ounkomol, C., Seshamani, S., Maleckar, M.M., Collman, F., and Johnson, G.R. (2018). Label-free prediction of three-dimensional fluorescence images from transmitted-light microscopy. Nat. Methods *15*, 917–920. https://doi.org/10.1038/s41592-018-0111-2.

18. Christiansen, E.M., Yang, S.J., Ando, D.M., Javaherian, A., Skibinski, G., Lipnick, S., Mount, E., O'Neil, A., Shah, K., Lee, A.K., et al. (2018). In Silico Labeling: Predicting Fluorescent Labels in Unlabeled Images. Cell *173*, 792–803. https://doi.org/10.1016/j.cell.2018.03.040.

19. Cross-Zamirski, J.O., Mouchet, E., Williams, G., Schönlieb, C.-B., Turkki, R., and Wang, Y. (2022). Label-free prediction of cell painting from brightfield images. Sci. Rep. *12*, 10001. https://doi.org/10.1038/s41598-022-12914-x.

20. Kok, R.N.U. (2023). LabelFreeTracker. https://github.com/jvzonlab/LabelFreeTracker.

21. Ronneberger, O., Fischer, P., and Brox, T. (2015). U-Net: Convolutional Networks for Biomedical Image Segmentation. In Medical Image Computing and Computer-Assisted Intervention – MICCAI 2015 Lecture Notes in Computer Science, N. Navab, J. Hornegger, W.M. Wells, and A.F. Frangi, eds. (Springer International Publishing), pp. 234–241. https://doi.org/10.1007/978-3-319-24574-4_28.

22. Çiçek, Ö., Abdulkadir, A., Lienkamp, S.S., Brox, T., and Ronneberger, O. (2016). 3D U-Net: Learning Dense Volumetric Segmentation from Sparse Annotation. In Medical Image Computing and Computer-Assisted Intervention – MICCAI 2016 Lecture Notes in Computer Science, S. Ourselin, L. Joskowicz, M.R. Sabuncu, G. Unal, and W. Wells, eds. (Springer International Publishing), pp. 424–432. https://doi.org/10.1007/978-3-319-46723-8_49.

23. Moosdijk, A.A.A., Grift, Y.B.C., Man, S.M.A., Zeeman, A.L., and Amerongen, R. (2020). A novel *Axin2* knock-in mouse model for visualization and lineage tracing of WNT/CTNNB1 responsive cells. Genesis *58*, 23387. https://doi.org/10.1002/dvg.23387.

24. Gregorieff, A., and Clevers, H. (2005). Wnt signaling in the intestinal epithelium: from endoderm to cancer. Genes Dev. *19*, 877–890. https://doi.org/10.1101/gad.1295405.

25. Skylaki, S., Hilsenbeck, O., and Schroeder, T. (2016). Challenges in long-term imaging and quantification of single-cell dynamics. Nat. Biotechnol. *34*, 1137–1144. https://doi.org/10.1038/nbt.3713.

26. Atwell, S., Waibel, D.J.E., Boushehri, S.S., Wiedenmann, S., Marr, C., and Meier, M. (2023). Label-free imaging of 3D pluripotent stem cell differentiation dynamics on chip. Cell Rep. Methods *3*, 100523. https://doi.org/10.1016/j.crmeth.2023.100523.

27. Sato, T., Vries, R.G., Snippert, H.J., van de Wetering, M., Barker, N., Stange, D.E., van Es, J.H., Abo, A., Kujala, P., Peters, P.J., and Clevers, H. (2009). Single Lgr5 stem cells build crypt-villus structures in vitro without a mesenchymal niche. Nature *459*, 262–265. https://doi.org/10.1038/nature07935.

28. Kingma, D.P., and Ba, J. (2017). Adam: A Method for Stochastic Optimization. Preprint at arXiv. https://doi.org/10.48550/arXiv.1412.6980.

29. Haubold, C., Aleš, J., Wolf, S., and Hamprecht, F.A. (2016). A Generalized Successive Shortest Paths Solver for Tracking Dividing Targets. In Computer Vision – ECCV 2016 Lecture Notes in Computer Science, B. Leibe, J. Matas, N. Sebe, and M. Welling, eds. (Springer International Publishing), pp. 566–582. https://doi.org/10.1007/978-3-319-46478-7_35.

30. Mahotas: Open source software for scriptable computer vision (2013). J. Open Res. Softw. 1, e3. https://doi.org/10.5334/jors.ac.

31. Hunter, J.D. (2007). Matplotlib: A 2D Graphics Environment. Comput. Sci. Eng. *9*, 90–95.

32. Abadi, M., Agarwal, A., Barham, P., Brevdo, E., Chen, Z., Citro, C., Corrado, G.S., Davis, A., Dean, J., Devin, M., et al. (2016). TensorFlow: Large-Scale Machine Learning on Heterogeneous Distributed Systems. Preprint at arXiv. https://doi.org/10.48550/arXiv.1603.04467.

33. Kok, R.N.U., Spoelstra, W.K., Betjes, M.A., van Zon, J.S., and Tans, S.J. (2025). LabelFreeTracker (Zenodo). https://doi.org/10.5281/zenodo.14814672.